9-13-2002

Construction, Pattern Recognition and Performance of the CLEO III LiF-TEA RICH Detector

Raymond Mountain
Syracuse University

R. Ayad
Syracuse University

Konstantin Vladimirovich Bukin
Syracuse University

A. Efimov
Syracuse University

Construction, Pattern Recognition and Performance of the CLEO III LiF-TEA RICH Detector

M. Artuso, R. Ayad, K. Bukin, A. Efimov, C. Boulahouache, E. Dambasuren, S. Kopp, R. Mountain, G. Majumder, S. Schuh, T. Skwarnicki, S. Stone, G. Viehhauser, J. C. Wang, and [a]
T. E. Coan, V. Fadeyev, Y. Maravin, I. Volobouev, J. Ye, and [b]
S. Anderson, Y. Kubota, and A. Smith [c]

[a]Syracuse University, Syracuse, NY 13244-1130, U. S. A.

[b]Southern Methodist University, Dallas, TX 75275-0175

[c]University of Minnesota, Minneapolis, MN 55455-0112

We briefly describe the design, construction and performance of the LiF-Tea RICH detector built to identify charged particles in the CLEO III experiment. Excellent π/K separation is demonstrated.

1. INTRODUCTION

1.1. The CLEO III Detector

The CLEO III detector was designed to study decays of b and c quarks, τ leptons and Υ mesons produced in e^+e^- collisions near 10 GeV center-of-mass energy. The new detector is an upgraded version of CLEO II [1]. It contains a new four-layer silicon strip vertex detector, a new wire drift chamber and a particle identification system based on the detection of Cherenkov ring images. Information about CLEO III is available elsewhere [2,3].

CLEO II produced many physics results, but was hampered by its limited charged-hadron identification capabilities. Design choices for particle identification were limited by radial space and the necessity of minimizing the material in front of the CsI crystal calorimeter. The CsI imposed a hard outer radial limit and the desire for maintaining excellent charged particle tracking imposed a lower limit, since at high momentum the error in momentum is proportional to the square of the track length. The particle identification system was allocated only 20 cm of radial space, and this limited the technology choices. We were also allowed a total material thickness corresponding to only 12% of a radiation length.

2. DETECTOR DESCRIPTION

2.1. Detector Elements

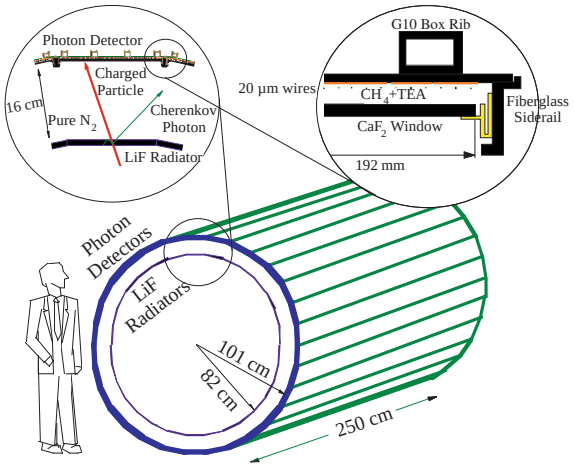

Figure 1. Outline of CLEO III RICH design.

The severe radial spatial requirement forces a thin, few cm detector for Cherenkov photons and a thin radiator. Otherwise the photons have little distance to travel and it becomes very difficult to precisely measure the photon angles. In fact, the only thin photon-detectors possible in our situation were wire chamber based, either CsI or

a mixture of triethylamine (TEA) and methane. Use of CsI would have allowed us to use a liquid freon radiator with quartz windows in the system using the optical wavelength region from about 160-200 nm. However, at the time of decision, the use of CsI was far from proven and, in any case, would have imposed severe constraints on the construction process which would have been both difficult and expensive. Thus we chose TEA + CH_4 and used Cherenkov photons between 135-165 nm generated in a 1 cm thick LiF crystal and used CaF_2 windows on our wire chambers (LiF windows were used on 10% of the chambers)[4].

Details of the design of the CLEO III RICH have been discussed before [5]. Here we briefly review the main elements. Cherenkov photons are produced in a LiF radiator. The photons then enter a free space, an "expansion volume," where the cone of Cherenkov light expands. Finally the photons enter a detector consisting of multi-wire proportional chambers filled with a mixture of TEA and CH_4 gases. No light focusing is used; this is called "proximity-focusing" [6]. The scheme is shown in the upper left of Fig. 1.

There are 30 photon detectors around the cylinder. They subtend the same azimuthal angle as the radiators, which are also segmented into 14 sections along their length of the cylinder. The gap between the radiators and detectors, called the "expansion gap", is filled with pure N_2 gas. The wire chamber design is shown in Fig. 1.

2.2. Radiators

LiF was chosen over CaF_2 or MgF_2, both of which are transparent in the useful wavelength region, because of smaller chromatic error. Originally all the radiators were planned to be 1 cm thick planar pieces. However, since the refractive index of LiF at 150 nm is 1.5, all the Cherenkov light from tracks normal to the LiF would be totally internally reflected as shown in Fig. 2 (top). We could have used these flat radiators, but we would have had to tilt them at about a 15° angle. Instead we developed radiators with striations in the top surface, called "sawtooth" radiators [7], as shown in Fig. 2 (bottom).

The overall radiator shape approximates a cylinder of radius 82 cm. Individual radiators

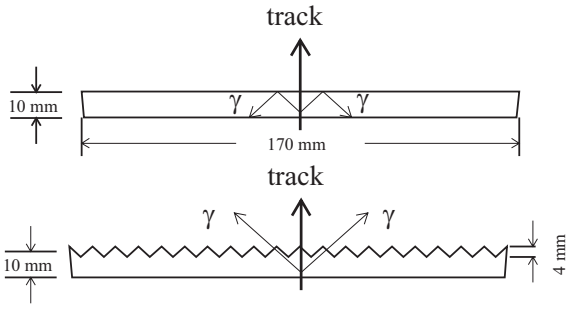

Figure 2. Sketch of a plane radiator (top) and a sawtooth radiator (bottom). Light paths radiated from a charged track normal to each radiator are shown.

are placed in 14 coaxial rings of 30 crystals each, centered around the beam line and symmetrically positioned about the interaction point. Only the inner four radiators are sawtooths.(The 30 crystals segments are parallel to the wire chambers.) Inter-crystal gaps are typically 50 μm. The crystals are attached to the exterior surface of a 1.5 mm thick carbon fiber shell with a low outgassing epoxy.

2.3. Photon Detectors

Construction was carried out in a class 100 clean room that was dehumidified below 35%. Granite tables were used that were flat over the entire surface of a photon detector module to better than 15 μm.

The photon detectors have segmented cathode pads 7.5 mm (length) x 8.0 mm (width) etched onto G10 boards. The pad array was formed from four individual boards, with 24 x 80 pads, with the latter separated into two 40 pad sections with a 6 mm gap. Each board was individually flattened in an oven and then they were glued together longitudinally on a granite table where reinforcing G10 ribs were also glued on. There are 4 longitudinal ribs that have a box structure. Smaller cross ribs are placed every 12 cm for extra stiffening. The total length was 2.4 m.

Wire planes were separately strung with 20 μm diameter gold plated tungsten with a 3% admixture of rhenium produced by LUMA; the wire pitch was 2.66 mm, for a total of 72 wires per chamber. The wires were placed on and subse-

quently glued to precision ceramic spacers 1 mm above the cathodes and 3.5 mm to the CaF_2 windows, every 30 cm. We achieved a tolerance of 50 μm on the wire to cathode distance. The spacers had slots in the center for the glue bead.

Eight 30 cm x 19 cm CaF_2 windows were glued together in precision jigs lengthwise to form a 2.4 m long window. Positive high voltage is applied to the anode wires, while - high voltage is put on 100 μm wide silver traces deposited on the CaF_2. The spacing between the traces is 2.5 mm. To maintain the ability of disconnecting any faulty part of a chamber, the wire HV is distributed independently to 3 groups of 24 wires and the windows are each powered separately.

2.4. Electronics

The position of Cherenkov photons is measured by sensing the induced charge on array of 7.5 mm x 8.0 mm cathode pads. Since the pulse height distribution from single photons is expected to be exponential at low to moderate gas gains [8], this requires the use of low noise electronics. Pad clusters in the detector can be formed from single Cherenkov photons, overlaps of more than one Cherenkov photon or charged tracks. In Fig. 3 we show the pulse height distribution for single photons, and charged tracks. We can distinguish somewhat between single photons hitting the pad array and two photons because of the pulse height shapes on adjacent pads. The charged tracks give very large pulse heights because they are traversing 4.5 mm of the CH_4-TEA mixture.

To have as low noise electronics as possible, a dedicated VLSI chip, called VA_RICH, based on a very successful chip developed for solid state applications, has been designed and produced for our application at IDE AS, Norway. We have fully characterized 3,600 64 channel chips, mounted on hybrid circuits. For moderate values of the input capacitance C_{in}, the equivalent noise charge measured ENC is found to be about:

$$ENC = 130e^- + (9e^-/\mathrm{pF}) \times C_{in} \quad . \qquad (1)$$

Its dynamic range is between 450,000 and 900,000 electrons, depending upon whether we choose a bias point for the output buffer suitable for signals of positive or negative polarity or we shift this

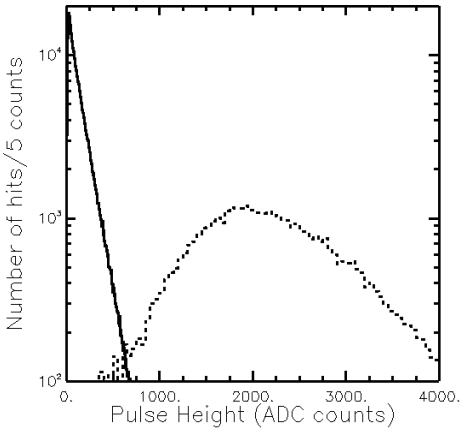

Figure 3. Pulse height distributions from pad clusters containing single photons (solid histogram) and charged tracks (dashed histogram). The line shows a fit of photon data to an exponential distribution. One ADC count corresponds to approximately 200 electrons. The charged track distribution is affected by electronic saturation. The wire voltage is +1.5 kV and the window voltage -1.2 kV.

bias point to have the maximum dynamic range for signals of a single polarity.

In our readout scheme we group 10 chips in a single readout cell communicating with data boards located in VME crates just outside the detector cylinder. Chips in the same readout cell share the same cable, which routes control signals and bias voltages from the data boards and output signals to the data boards. Two VA_RICH chips are mounted using wire bonds on one hybrid circuit that is attached via two miniature connectors to the back of the cathode board of the photon detector.

The analog output of the VA_RICH is transmitted to the data boards as a differential current, transformed into a voltage by transimpedance amplifiers and digitized by a 12 bit differential ADC. These receivers are part of very complex data boards which perform several important analog and digital functions. Each board contains 15 digitization circuits and three analog power supply sections providing the voltages and currents to bias the chips, and calibration circuitry. The digital component of these boards contains a

sparsification circuit, an event buffer, memory to store the pedestal values, and the interface to the VME cpu.

Coherent noise is present. We eliminate this by measuring the pulse heights on all the channels and performing an average of the non-struck channels before the data sparsification step [9]. The pedestal width (rms) changes from 3.6 to 2.5 channels with and without this coherent noise subtraction, respectively. The total noise of the system then is ∼500 electrons rms.

2.5. Gas System

The gas system supplies several distinct volumes. The systems must: supply CH_4-TEA to 30 separate chambers, supply super-clean N_2 to the expansion gap, supply super-clean N_2 to a sealed single volume surrounding all the chambers, called the electronics volume, since this is the region where the front-end hybrid boards are present. In addition we need to test CH_4-TEA for the ability to detect photons and test the output N_2 for purity.

It is of primary importance that the gas system must NOT destroy any of the thin CaF_2 windows. We use computerized pressure and flow sensors with PLC controllers. The gas system works great. N_2 transparency is >99%. Nothing has been broken!

3. OPERATING EXPERIENCE

The detector has been in operation since September of 1999. All but ∼2% of the detector is functioning. We lost 1% due to the breaking of one wire after about one year of operation. We have also lost 2% of the electronics chips.

4. OFF-LINE DATA ANALYSIS AND PHYSICS PERFORMANCE

4.1. Noise filtering

Coherent noise suppression and data sparsification are performed on-line to eliminate the Gaussian part of the electric noise. A small non-Gaussian component of the coherent electric noise is eliminated off-line, by using an algorithm too complicated for use in the data board DSP. The incoherent part of non-Gaussian noise was eliminated by off-line pulse height thresholds adjusted to keep occupancy of each channel below 1%. Finally we eliminate clusters of cathode pad hits that are extended along the anode wires, but are only 1-2 pads wide in the other direction.

4.2. Cherenkov Images

We show in Fig. 4 the hit pattern in the detector for a Bhabha scattering event ($e^+e^- \to e^+e^-$) for track entering the plane (left image) and sawtooth (right image) radiators. The shapes of the Cherenkov "rings" are different in the two cases, resulting from refraction when leaving the LiF radiators. The hits in the centers of the images are produced by the electron passing the RICH MWPC.

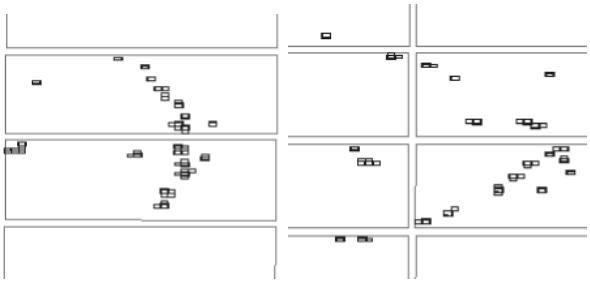

Figure 4. Hit patterns produced by the particle passing through the plane (left) and sawtooth (right) radiators.

4.3. Clustering of Hits

The entire detector contains 230,400 cathode pads, which are segmented into 240 modules of 24×48 pads separated by the mounting rails and anode wire spacers. We cluster pad hits in each module separately. Pad hits touching each other either by a side or a corner form a "connected region." Each charged track reconstructed in the CLEO-III tracking system [10] is projected onto the RICH MWPC and matched to the closest connected region. If the matching distance between the track projection and the connected region center is reasonably small and the total pulse height of the connected region sufficiently high we associate this group of hits with the track. Local pulse height maxima in the remaining connected regions, so called "bumps" are taken as seeds for Cherenkov photons. We allow the pulse

height maxima to touch each other by corners if the pulse height in the two neighboring pads is small relative to both bump hits. Hits adjacent to the bumps on the sides are assigned to them in order of decreasing bump pulse height.

To estimate the position of the photon conversion point we use the center-of-gravity method corrected for the bias towards the central pad. For many Cherenkov photons we are able to detect induced charge in only one pad. Since the pad dimensions are about 8×8 mm^2, the position resolution in this case is $8/\sqrt{12} = 2.3$ mm. For charged track intersections, which induce significant charge in many pads, the position resolution is 0.76 mm. The position resolution for Cherenkov photons which generate multiple pad hits is somewhere in between these two values. In any case, the photon position error is not a significant contribution to the Cherenkov angle resolution (see below).

4.4. Corrections to the Track Direction

The resolution of the CLEO-III tracking system is very good in the bending view (the magnetic field is solenoidal in CLEO) [10] . The track position and inclination angle along the beam axis is measured less precisely, with the silicon vertex detector playing the dominant role. The rms of the observed RICH hit residual is 1.7 mm. Since the RICH hit position resolution is 0.76 mm as measured by the residual in the perpendicular direction, the RICH MWPC can clearly help in pinning down the track trajectory. This, in turn, improves Cherenkov resolution, especially for the flat radiators for which we observe only half of the Cherenkov image and thus are quite sensitive to the tracking error. The improvement is as much as 50% is some parts of the detector.

4.5. Reconstruction of Cherenkov Angle

Given the measured position of the Cherenkov photon conversion point in the RICH MWPC, the charged track direction and its intersection point with the LiF radiator, we calculate a Cherenkov angle for each photon-track combination (θ_γ). We use the formalism outlined by Ypsilantis and Séguinot [6], except that we adopt a numerical method to find the solution to the equation for the photon direction, instead of simplifying it to a 4^{th} order polynomial, which would allow an analytical solution, but at the expense of introducing an additional source of error. Furthermore, using our numerical method, we calculate derivatives of the Cherenkov angle with respect to the measured quantities which allows us to propagate the detector errors and the chromatic dispersion to obtain an expected Cherenkov photon resolution for each photon independently (σ_θ). This is useful, since the Cherenkov angle resolution varies significantly even within one Cherenkov image. We use these estimated errors when calculating particle ID likelihoods and use them as to weight each photon when considering the average Cherenkov angle for a track.

4.6. Performance on Bhabha Events

We first view the physics performance on the simplest type of events, Bhabha events and then subsequently in hadronic events. The Cherenkov angle measured for each photon is shown in Fig. 5.

We note that Bhabha events are very low multiplicity compared with our normal hadronic events. They have two charged tracks present while the hadronic events have an average charged multiplicity of approximately 10. In addition, the hadronic events have on the average 10 photons, mainly from π^o decays. All of these particles can interact in the calorimeter and the splash-back can hit the RICH photon detector.

This Cherenkov angle spectrum for single photons has an asymmetric tail and modest background. It is fit with a line-shape similar to that used by for extracting photon signals from electromagnetic calorimeters [11]. The functional form is

$$P(\theta|\theta_{exp},\sigma_\theta,\alpha,n) = \qquad (2)$$

$$\begin{cases} A \cdot \exp\left[-\frac{1}{2}\left(\frac{\theta_{exp}-\theta}{\sigma_\theta}\right)^2\right] & \text{for } \theta < \theta_{exp} - \alpha\cdot\sigma_\theta \\ A \cdot \frac{\left(\frac{n}{\alpha}\right)^n e^{-\frac{1}{2}\alpha^2}}{\left(\frac{\theta_{exp}-\theta}{\sigma_\theta}+\frac{n}{\alpha}-\alpha\right)^n} & \text{for } \theta > \theta_{exp} - \alpha\cdot\sigma_\theta, \end{cases}$$

$$A^{-1} \equiv \sigma_\theta\left[\frac{n}{\alpha}\frac{1}{n-1}e^{-\frac{1}{2}\alpha^2} + \sqrt{\frac{\pi}{2}}\left(1+\mathrm{erf}\left(\frac{\alpha}{\sqrt{2}}\right)\right)\right].$$

Here θ is the measured angle, θ_{exp} is the "true" (or most likely) angle and σ_θ is the angular res-

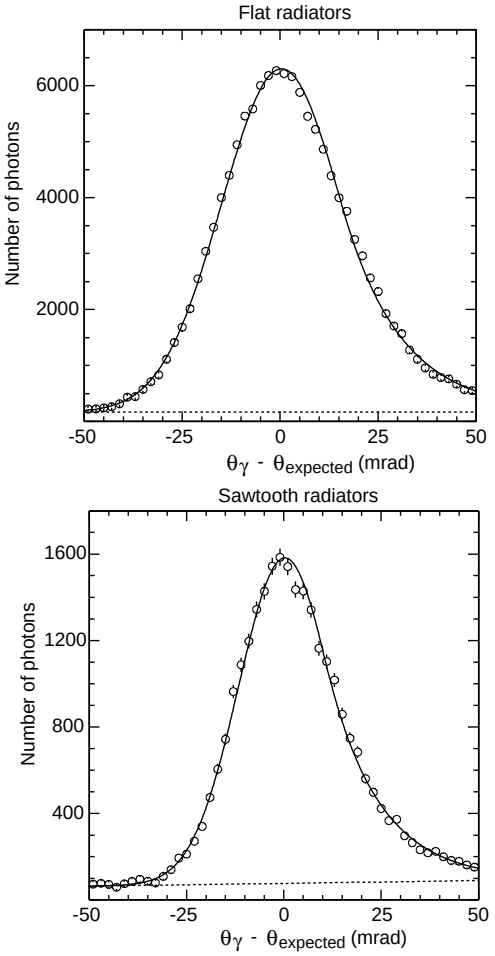

Figure 5. The measured minus expected Cherenkov angle for each photon detected in Bhabha events, (top) for plane radiators and (bottom) for sawtooth radiators. The curves are fits to special line shape function (see text), while the lines are fits to a background polynomial.

olution. To use this formula, the parameter n is fixed to value of about 5.

The data in Fig. 5 are fit using this signal shape plus a polynomial background function. We compare the results of these fits for the resolution parameter σ_θ as a function of radiator ring for data and Monte Carlo simulation in Fig. 6. The single photon resolution averaged over the detector solid angles are 14.7 mr for the flat radiator and 12.2 mr for the sawtooth.

The number of photons per track within a $\pm 3\sigma$ of the expected Cherenkov angle for each photon

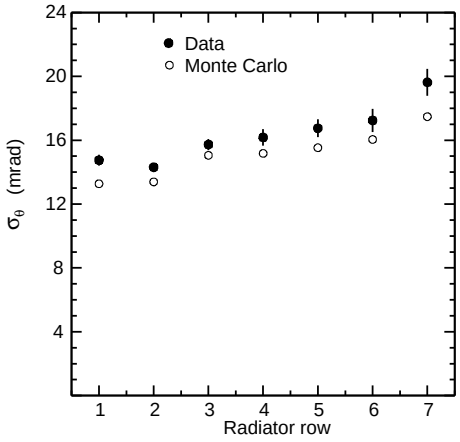

Figure 6. The values of the angular resolution for single photons for data compared with Monte Carlo simulation as a function of radiator ring. Sawtooth radiators are in rings 1 and 2, near the center of the detector.

is shown in Fig. 7 and shown as a function of radiator ring in Fig. 8. Averaged over the detector, and subtracting the background we have a mean number of 10.6 photons with the flat radiators and 11.9 using the sawtooth radiators.

The resolution per track is obtained by taking a slice within $\pm 3\sigma$ of the expected Cherenkov angle for each photon and forming an average weighted by $1/\sigma_\theta^2$. These track angles are shown in Fig. 9.

The rms spreads of these distributions are identified as the track resolutions. We obtain 4.7 mr for the flat radiators and 3.6 mr for the sawtooth. The resolutions as a function of radiator ring are shown in Fig. 10.

The Cherenkov angular resolution is comprised of several different components. This include error on the location of the photon emission point, the chromatic dispersion, the position error in the reconstruction of the detected photons and finally the error on determining the charged track's direction and position. These components are compared with the data in Fig. 11.

4.7. Performance on Hadronic Events

To resolve overlaps between Cherenkov images for different tracks we find the most likely mass hypotheses. Photons that match the most hy-

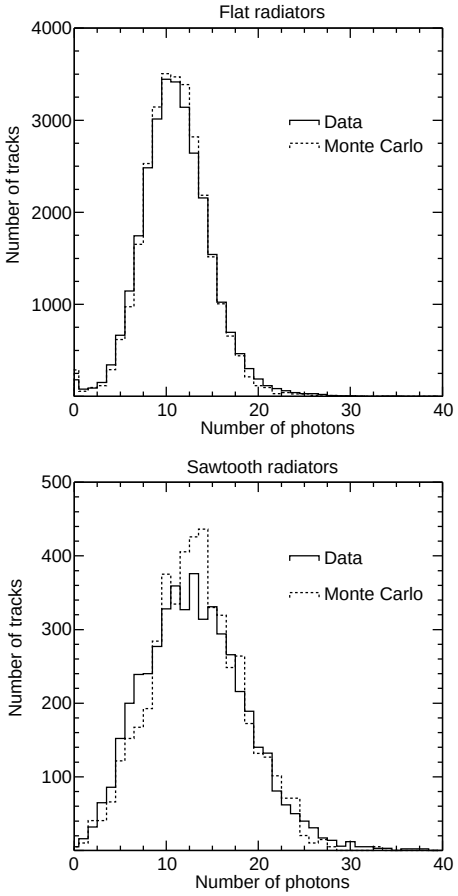

Figure 7. The number of photons detected on Bhabha tracks (top) for plane radiators and (bottom) for sawtooth radiators. The dashed lines are predictions of the Monte Carlo simulation.

pothesis within $\pm 3\sigma$ are then removed from consideration for the other tracks. To study the RICH performance in hadronic events we use $D^{*+} \to \pi^+ D^0$, $D^0 \to K^-\pi^+$ events. The charge of the slow pion in the D^{*+} decay is opposite to the kaon charge in subsequent D^0 decay. Therefore, the kaon and pion in the D^0 decay can be identified without use of the RICH detector. The effect of the small combinatorial background is eliminated by fitting the D^0 mass peak in the $K^+\pi^-$ mass distribution to obtain the number of signal events for each momentum bin.

Single-photon Cherenkov angle distributions obtained on such identified kaons with the momentum above 0.7 GeV/c are plotted in Fig. 12. Averaged over all radiators, the single-photon resolution is 13.2 mr and 15.1 mr for sawtooth and flat radiators respectively. The background fraction within $\pm 3\sigma$ of the expected value is 12.8% and 8.4%. The background-subtracted mean photon yield is 11.8 and 9.6. Finally the per-track Cherenkov angle resolution is 3.7 mr and 4.9 mr.

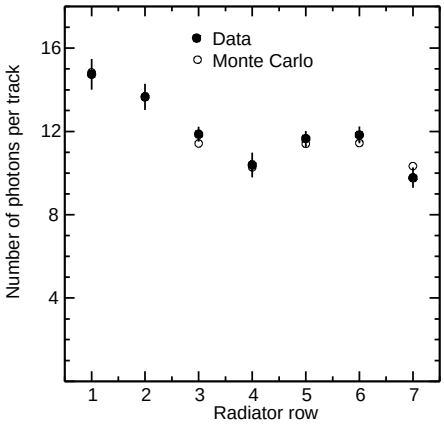

Figure 8. The number of photons as a function of radiator ring.

4.8. Particle ID Likelihoods

For parts of the Cherenkov image for the sawtooth radiator, and for tracks intersecting more than one radiator there are some optical path ambiguities that impact the Cherenkov angle calculations. In the previous section we bypassed this problem by selecting the optical path that produces the closest Cherenkov angle to the expected one (θ^h_{exp}) for the given particle hypothesis (h). There is some loss of information in this procedure, therefore, we use the likelihood method to perform particle identification instead of the per-track average angle. The likelihood method weights each possible optical path by the optical probability (P_{opt}), which includes length of the radiation path and the refraction probabilities obtained by the inverse ray tracing method:

$$L_h = \prod_{j=1}^{No.\,of\,\gamma s} \Big\{ P_{background} +$$

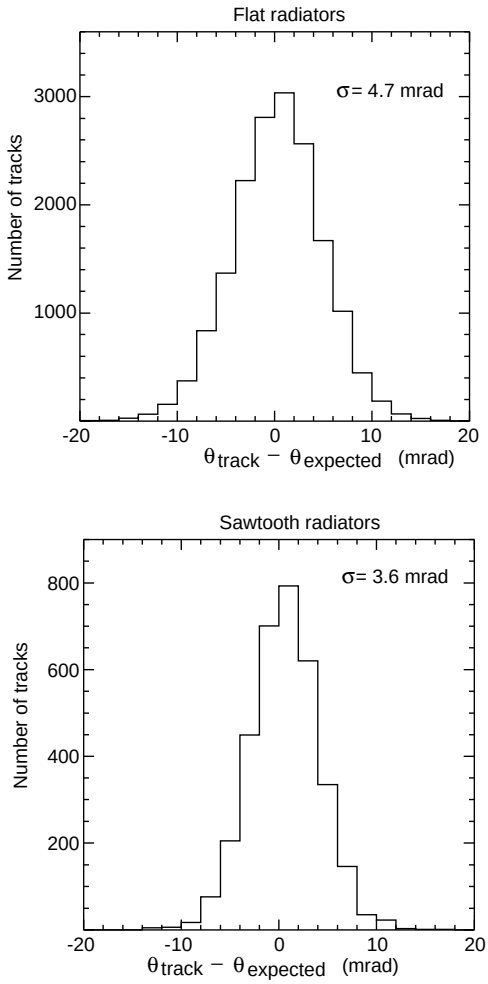

Figure 9. Track resolutions in Bhabha events, (left) for plane radiators and (right) for sawtooth radiators.

$$\sum_{opt} P^{j}_{opt} \cdot P_{signal}\left(\theta^{opt,\,j}_{\gamma} | \theta^{h}_{exp},\, \sigma^{opt,\,j}_{\theta}\right)\Bigg\}$$

where, L_h is the likelihood for the particle hypothesis h (e, μ, π, K or p), $P_{background}$ is the background probability approximated by a constant and P_{signal} is the signal probability given by the line-shape defined previously. In principle, the likelihood could include all hits in the detector. In practice, there is no point in inspecting hits which are far away from the regions where photons are expected for at least one of the considered hypotheses (we use $\pm 5\sigma$ cut-off).

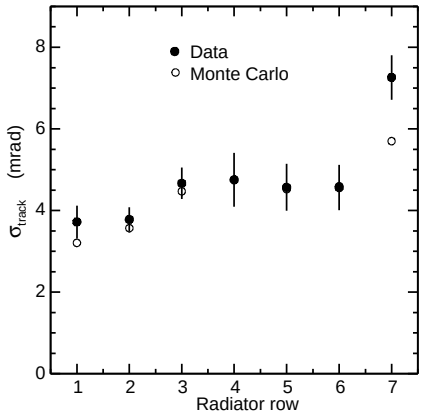

Figure 10. Cherenkov angle resolutions per track as a function of radiator ring for Bhabha events.

An arbitrary scale factor in the likelihood definition cancels when we consider likelihood ratios for two different hypotheses. The likelihood conveniently folds in information about values of the Cherenkov angles and the photon yield for each hypothesis. For well separated hypotheses (typically at lower momenta) it is the photon yield that provides the discrimination. For hypotheses that produce Cherenkov images in the same area of the detector, the values of the Cherenkov angles do the job. Since our likelihood definition does not know about the radiation momentum threshold, the likelihood ratio method can be only used when both hypotheses are sufficiently above the thresholds. When one hypothesis is below the radiation threshold we use a value of the likelihood for the hypothesis above the threshold to perform the discrimination.

The distribution of the $2\ln(L_\pi/L_K)$, is expected to behave as the difference $\chi^2_K - \chi^2_\pi$. This χ^2 difference obtained for 1.0-1.5 GeV/c kaons and pions identified with the D^* method is plotted in Fig. 13. Cuts at different values of this variable produce identification with different efficiency and fake rate. Pion fake rate for different values of kaon identification efficiency is plotted as a function of particle momentum in Fig. 14.

4.9. Conclusions

We have successfully constructed and operated a large, complex RICH detector in a particle physics experiment for over three years. About

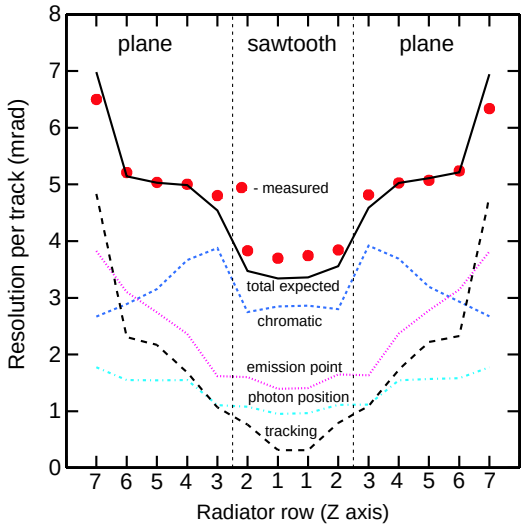

Figure 11. Different components of the Cherenkov angle resolutions per track as a function of radiator ring for Bhabha events. The points are the data and the solid line is the sum of the predicted resolution from each of the components indicated on the figure.

98% of the detector is operational (1% loss due to one broken wire and 1% due to electronic failures).

The particle momenta for B meson decay products seen by CLEO are less than 2.65 GeV/c. The detector provides excellent separation between pions and kaons at and below this cutoff. Separation between kaons and protons extends to even higher momentum, where it is used in charm baryon studies. Thus, the physics performance has met design criteria.

CLEO currently is making an extensive study of Upsilon decays and proposes to study decays of charm mesons and charmonium decays (called CLEO-c [12]). For these measurements the beam energy will be lowered and the maximum particle momenta will be about 1.5 GeV/c. At these momentum the particle identification fake rates are at the 1% level.

4.10. Acknowledgments

This work was supported by the U. S. National Science Foundation and Department of Energy. We thank Tom Ypsilantis and Jacques Séguinot for suggesting the basic technique. We thank the accelerator group at CESR for excellent efforts in supplying luminosity.

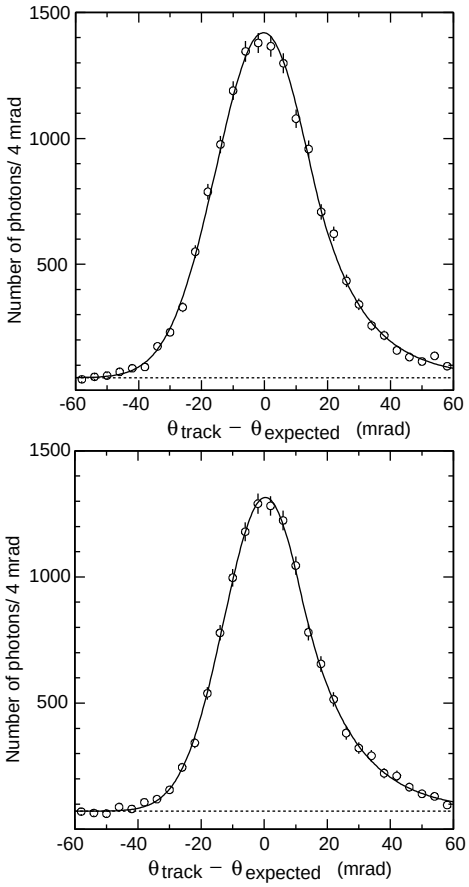

Figure 12. The measured minus expected Cherenkov angle for each photon detected in hadronic events, (top) for plane radiators and (bottom) for sawtooth radiators. The curves are fits to special line shape function (see text), while the lines are fits to a background polynomial.

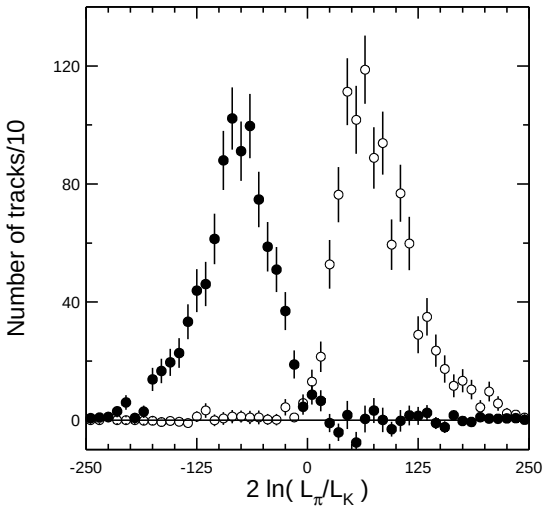

Figure 13. Distribution of $2\ln(L_\pi/L_K) \sim \chi^2_K - \chi^2_\pi$ for 1.0-1.5 GeV/c kaons (filled) and pions (open) identified with the D^* method.

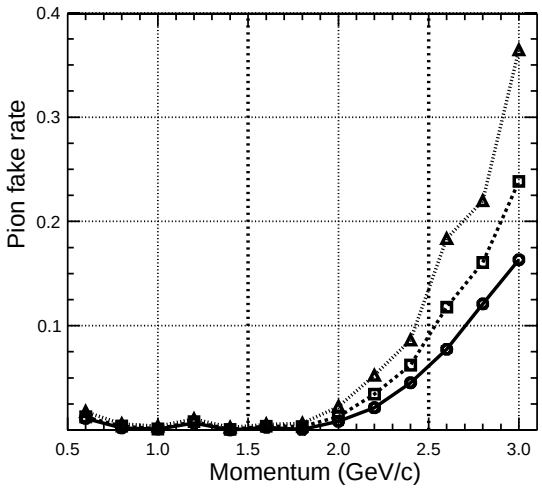

Figure 14. Pion fake rate as a function of particle momentum for kaon efficiency of 80% (circles), 85% (squares) and 90% (triangles).

REFERENCES

1. Y. Kubota *et al*, Nucl. Instr. Meth. A320 (1992) 66.
2. M. Artuso, "Progress Towards CLEO III", in the Proceedings of the XXIX International Conference on High Energy Physics, Vancouver, Ed. by A. Astbury et al., World Scientific, Singapore, vol. 2, p 1552, [hep-ex/9811031] (1998).
3. S.E. Kopp, Nucl. Instr. Meth. A384 (1996) 61.
4. A similar system was tested previously, see R. Arnold et al., Nucl. Instr. Meth. A314 (1992) 465; J.-L. Guyonnet et al., Nucl. Instr. Meth. A343 (1994) 178; J. Séguinot et al., Nucl. Instr. Meth. A350 (1994) 430.
5. M. Artuso et al., Nucl. Instr. Meth. A441 (2000) 374-392
6. T. Ypsilantis and J. Séguinot, Nucl. Instr. Meth. A343 (1994) 30.
7. A. Efimov and S. Stone, Nucl. Instr. and Meth. A371 (1996) 79.
8. R. Bouclier et al., Nucl. Instr. Meth. A205 (1983) 205.
9. This alorithim is executed by a DSP located on the data boards before the data are sparsified.
10. D. Peterson et al., Nucl. Instr. Meth. A478 (2002) 142.
11. T. Skwarnicki, "A Study of the Radiative Cascade Transitions Between the Upsilon-Prime and Upsilon Resonances," DESY F31-86-02 (thesis, unpublished) (1986).
12. I. Shipsey, "CLEO-c and CESR-c: Allowing Quark Flavor Physics to Reach its Full Potential," to appear in the proceedings of Flavor Physics and CP Violation (FPCP) May, 2002. Univ. of Pennsylvania, Philadelphia, PA, [hep-ex/0207091] (2002).